Multisideband interference structures observed via high-order photon-induced continuum-continuum transitions in argon

D. Bharti, ¹, ¹, H. Srinivas, ¹ F. Shobeiry, ¹ K. R. Hamilton, ², ², R. Moshammer, ¹ T. Pfeifer, ¹ K. Bartschat, ², ² and A. Harth, ^{1,4,*} ¹Max-Planck-Institute for Nuclear Physics, D-69117 Heidelberg, Germany

(Received 18 October 2022; accepted 19 January 2023; published 6 February 2023)

We report a joint experimental and theoretical study of a three-sideband (3-SB) modification of the reconstruction of attosecond beating by interference of two-photon transitions (RABBIT) setup. The 3-SB RABBIT scheme makes it possible to investigate phases resulting from interference between transitions of different orders in the continuum. Furthermore, the strength of this method is its ability to focus on the atomic phases only, independent of a chirp in the harmonics, by comparing the RABBIT phases extracted from specific SB groups formed by two adjacent harmonics. We verify earlier predictions that the phases and the corresponding time delays in the three SBs extracted from angle-integrated measurements become similar with increasing photoelectron energy. A variation in the angle dependence of the RABBIT phases in the three SBs results from the distinct Wigner and continuum-continuum coupling phases associated with the individual angular-momentum channels. A qualitative explanation of this dependence is attempted by invoking a propensity rule. Comparison between the experimental data and predictions from an R matrix (close-coupling) with time dependence calculation shows qualitative agreement in most of the observed trends.

DOI: 10.1103/PhysRevA.107.022801

I. INTRODUCTION

The reconstruction of attosecond beating by interference of two-photon transitions (RABBIT) is a widely employed technique to measure attosecond time delays in photoionization processes [1-3]. The extraction of time information from the RABBIT measurements usually involves retrieving atomic phases encoded in the delay-dependent modulation of the sideband (SB) yield. These SBs are traditionally formed in the photoelectron spectrum by the interaction of two photons (one pump, one probe) with the target. Spectral harmonics from an attosecond pulse train (the pump photons) form discrete photoelectron signal peaks. The presence of a time-delayed infrared field (the probe photon) then creates a signal between these main peaks that oscillates with the time delay. The so-retrieved atomic phase $(\Delta \phi^{at})$ from the RABBIT measurement can be separated into a singlephoton ionization contribution ($\Delta \eta$, Wigner phase [4]) and a continuum-continuum (cc) coupling phase $(\Delta \phi^{cc})$ by applying an asymptotic approximation [5-7].

Variations of the RABBIT scheme, such as 0-SB, 1-SB, and 2-SB, have been utilized to study dipole transition phases

Published by the American Physical Society under the terms of the Creative Commons Attribution 4.0 International license. Further distribution of this work must maintain attribution to the author(s) and the published article's title, journal citation, and DOI. Open access publication funded by the Max Planck Society.

and attosecond pulse shaping [8–10]. As the name suggests, in a 3-SB RABBIT scheme, three SBs are formed between two consecutive main photoelectron peaks [11,12]. The delaydependent oscillation in the photoelectron signal of these three SBs requires more than one transition in the continuum, i.e., the absorption or emission of several probe photons. For a hydrogenic system, we recently [12] extended the asymptotic approximation to a decomposition scheme, which expands the phase of the Nth-order dipole matrix element $\mathcal{M}^{(N)}$, describing the absorption of an ionizing extreme ultraviolet (XUV) photon followed by N-1 infrared (IR) photon exchanges in the continuum, into a sum of the Wigner phase and N-1 cc phases.

For atomic hydrogen, where numerical calculations with high accuracy can be carried out by solving the timedependent Schrödinger equation (TDSE) directly, we verified that the decomposition approximation explains the RABBIT phases in all three SBs qualitatively [12]. As expected, its accuracy improves with increasing energy of the emitted photoelectron. On the other hand, assuming $\Delta \phi^{cc}$ to be independent of the orbital angular momenta of the continuum states leads to deviations from the analytical prediction, particularly in the lower and the higher SB of the triplet at low kinetic energies.

Even though starting with a 3p electron still limits the information that can be extracted due to the combined effect of at least two Wigner and the cc phases, we decided to perform the present proof-of-principle study on argon due to its experimental advantages, including a significantly lower ionization potential than helium, which may be a viable alternative to atomic hydrogen due to its quasi-one-electron character, as

²Department of Physics and Astronomy, Drake University, Des Moines, Iowa 50311, USA

³Department of Physics. University of Colorado Denver, Denver, Colorado 80217, USA

⁴Department of Optics and Mechatronics, Hochschule Aalen, D-73430 Aalen, Germany

^{*}bharti@mpi-hd.mpg.de; anne.harth@hs-aalen.de

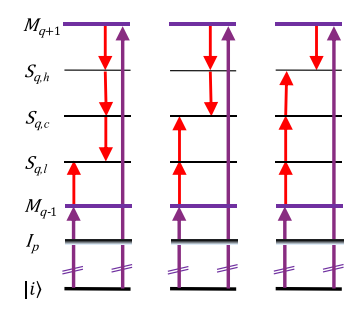


FIG. 1. 3-SB RABBIT scheme. M_{q-1} and M_{q+1} label the main photoelectron peaks created directly by the odd harmonics (H_{q-1} and H_{q+1}) of the frequency-doubled fundamental probe frequency in the XUV pulse, while $S_{q,l}$, $S_{q,c}$, and $S_{q,h}$ are the lower, central, and higher SBs, respectively. These SBs are formed by emission or absorption of probe photons by the quasi-free photoelectrons. $|i\rangle$ denotes the initial state and I_p is the ionization potential.

long as one of the electrons remains in the 1s orbital, i.e., away from doubly–excited resonance states. In argon, the intermediate orbital angular momentum after the XUV step is $\lambda = 0$ or 2, while $\lambda = 1$ in helium. For the latter target, as for atomic hydrogen, the dependence on the Wigner phase would drop out, and the 3-SB setup would provide direct access to the phase associated with higher-order cc transitions [11,12]. Nevertheless, a significant strength of our current setup already lies in the fact that the results within each group are *independent of any chirp* in the XUV pulse, because the XUV harmonic pair is common to all three SBs.

This paper is organized as follows. We begin with a brief review of the basic idea behind the 3-SB setup in Sec. II. This is followed by a description of the experimental apparatus in Sec. III and the accompanying theoretical *R* matrix (close-coupling) with time dependence (RMT) approach in Sec. IV. In Sec. V, we first show angle-integrated data (Sec. V A) before focusing on the angle dependence of the RABBIT phases in the three SBs of each individual group in Sec. V B. We finish with a summary and an outlook in Sec. VI.

II. THE 3-SB SCHEME

In this section, we briefly review the 3-SB scheme introduced in Ref. [11] and the analytical treatment presented in Ref. [12] as applied to the 3-SB RABBIT experiment.

Figure 1 illustrates only the two most dominant transition paths for each SB contributing to the oscillation in their respective yields. The lowest-order transition dominates the yield, but its modulation requires interference between at least two distinct paths leading to the same energy. This involves two different XUV harmonics that are aided by absorption or emission of near-infrared (NIR) photons. For the lower (l) and higher (h) SBs, S_l and S_h , the most important interfering paths are of second (one harmonic and one NIR) and fourth (one harmonic and three NIR) order, which results in a weak modulation of the yield. The lowest-order terms contributing to the buildup of the central (c) SB, S_c , are both of third order (one harmonic and two NIR). Consequently, interference between them exhibits the delay-dependent oscillation most clearly.

Mathematically, the angle-integrated yield in the three SBs, considering only two prominent transition paths, can be written as

$$\begin{split} S_{q,l} &\propto \sum_{\ell,m} \left| \left(\tilde{E}_{q+1} \tilde{E}_{\omega}^{*3} \mathcal{M}_{\ell,m}^{(4,e)}(k_{l,q}) + \tilde{E}_{q-1} \tilde{E}_{\omega} \mathcal{M}_{\ell,m}^{(2,a)}(k_{l,q}) \right) \right|^{2} \\ &= I_{0}^{l} + \sum_{\ell,m} I_{\ell,m}^{l} \cos \left(4 \,\omega \tau - \Delta \phi_{\Omega}^{q} - \Delta \phi_{\ell,m}^{l,at} \right) \\ &= I_{0}^{l} + I_{1}^{l} \cos \left(4 \,\omega \tau - \phi_{R}^{l} + \pi \right); \qquad (1a) \\ S_{q,c} &\propto \sum_{\ell,m} \left| \left(\tilde{E}_{q+1} \tilde{E}_{\omega}^{*2} \mathcal{M}_{\ell,m}^{(3,e)}(k_{c,q}) + \tilde{E}_{q-1} \tilde{E}_{\omega}^{2} \mathcal{M}_{\ell,m}^{(3,a)}(k_{c,q}) \right) \right|^{2} \\ &= I_{0}^{c} + \sum_{\ell,m} I_{\ell,m}^{c} \cos \left(4 \,\omega \tau - \Delta \phi_{\Omega}^{q} - \Delta \phi_{\ell,m}^{c,at} \right) \\ &= I_{0}^{c} + I_{1}^{c} \cos \left(4 \,\omega \tau - \phi_{R}^{c} \right); \qquad (1b) \\ S_{q,h} &\propto \sum_{\ell,m} \left| \left(\tilde{E}_{q+1} \tilde{E}_{\omega}^{*} \mathcal{M}_{\ell,m}^{(2,e)}(k_{h,q}) + \tilde{E}_{q-1} \tilde{E}_{\omega}^{3} \mathcal{M}_{\ell,m}^{(4,a)}(k_{h,q}) \right) \right|^{2} \\ &= I_{0}^{h} + \sum_{\ell,m} I_{\ell,m}^{h} \cos \left(4 \,\omega \tau - \Delta \phi_{\Omega}^{q} - \Delta \phi_{\ell,m}^{h,at} \right) \\ &= I_{0}^{h} + I_{1}^{h} \cos \left(4 \,\omega \tau - \phi_{R}^{h} + \pi \right). \qquad (1c) \end{split}$$

Here q labels the SB group, while $k_{l,q}$, $k_{c,q}$, and $k_{h,q}$ denote the final linear momenta of the ejected electron in the lower, central, and higher sidebands in each group. The subscript ℓ denotes one of generally several allowed orbital angular momenta of the ejected electron in the final state and m labels the magnetic quantum number, which can be 0 or ± 1 for the electron starting in the 3p subshell. Note that m is a conserved quantity for all orders n of the transition matrix element $\mathcal{M}_{\ell,m}^{(n)}$ due to our use of linearly polarized light.

Furthermore, $\tilde{E}_{\Omega} = E_{\Omega} \mathrm{e}^{i\,\phi_{\Omega}}$ and $\tilde{E}_{\omega} = E_{\omega} \mathrm{e}^{i\,\omega_{T}}$ (for absorption) are the complex electric-field amplitudes of the colinearly polarized XUV-pump (Ω) and NIR-probe (ω) pulses, respectively. $\Delta\phi_{\ell,m}^{\mathrm{at}} = \arg[\mathcal{M}_{\ell,m}^{(a)}\mathcal{M}_{\ell,m}^{*(e)}]$ is the phase difference between the two matrix elements and a(e) denotes the pathway involving absorption (emission) of the probe photons. Finally, $\Delta\phi_{\Omega}^{q}$ is the spectral phase difference (XUV chirp) of two neighboring harmonics.

As seen from Eqs. (1), the yield of each SB is separated into an average part I_0 and another term I_1 that oscillates at 4ω with the delay. As discussed in Ref. [12], every dipole transition also adds a phase of $\pi/2$. Since the two dominant interfering terms in S_l and S_h are of different orders (second and fourth), this leads to an additional π phase in S_l and S_h relative to S_c , where both interfering terms are of the same (third) order.

The RABBIT phase (ϕ_R) includes the spectral phase difference of the two harmonics and the channel-resolved atomic phases weighted according to their transition amplitudes. It is a complex inverse trigonometric function involving many parameters and hence is best determined by fitting the signal to the known analytic form given above. Since the three SBs involve the same pair of harmonics, the contribution of the XUV group delay (i.e., the chirp) to the oscillation phase is the same in all three SBs. This is a key advantage of the 3-SB method, since it removes the influence of the XUV chirp

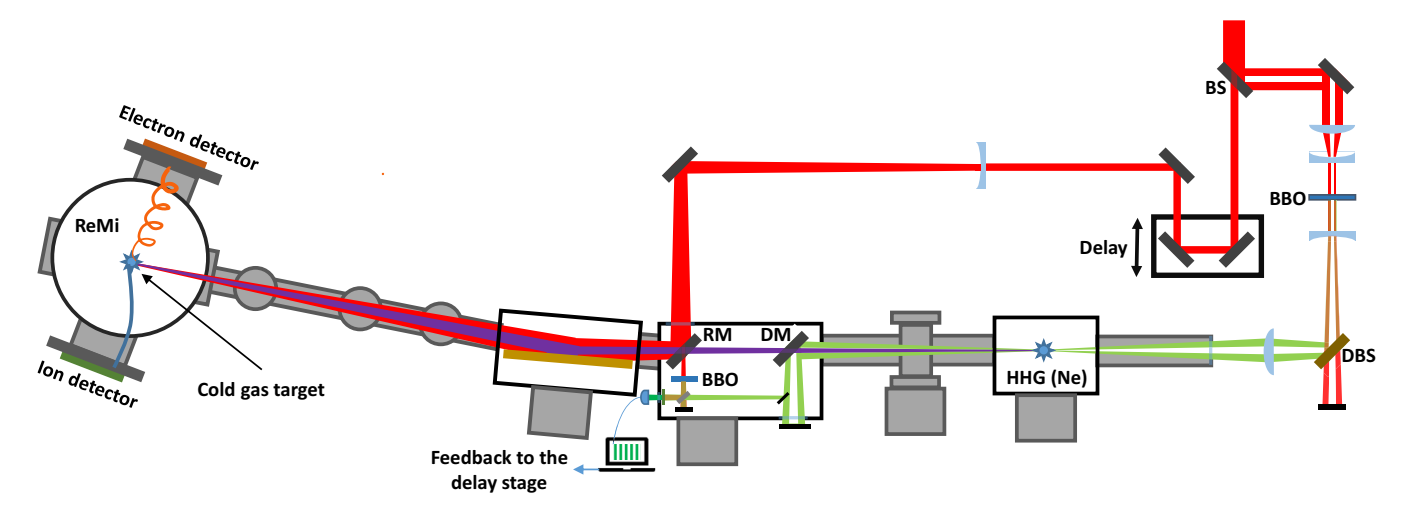


FIG. 2. Experimental setup. A holey mirror (BS) splits the linearly polarized laser beam between the two arms of the interferometer. In the pump arm, the HHG process is driven by the second harmonic of the laser beam. The generated XUV and the fundamental probe beam are recombined and focused onto a supersonic gas jet of argon. The interferometer is stabilized by tracking the movement of the fringes from the pump and the probe beams.

when we compare the phases of the three SBs only within a particular group.

III. EXPERIMENTAL SETUP

Figure 2 shows the schematic design of our 3-SB RABBIT experimental setup. A commercial fiber-based laser delivers pulses with a duration of approximately 50 fs [full width at half maximum (FWHM)] at a 49 kHz repetition rate with a pulse energy of 1.2 mJ and a center wavelength of 1030 nm. This pulse is split into two parts using a holey mirror (BS) that reflects $\sim\!85\%$ of the incoming beam in the pump arm, while the rest passes through the hole into the probe arm. The beam size of the reflected donut beam in the pump arm is reduced by a pair of lenses and passed through a 0.5-mm-thick Beta Barium Borate (BBO) crystal to double its frequency.

The conversion efficiency for the second-harmonic generation (SHG) by the BBO crystal is 25%-30%. A dichroic beam-splitter (DBS) filters out the fundamental beam, and a lens with a focal length of 12 cm focuses the second harmonic beam inside a vacuum chamber to a focal spot of $30-40 \,\mu\mathrm{m}$ on a jet of neon gas, which results in an XUV frequency comb through high-harmonic generation (HHG). The gas nozzle has a diameter of 100 µm and is operated at a backing pressure of 1.2 bar with a chamber pressure of 5×10^{-3} mbar. The generated XUV beam is spatially separated from the annular second harmonic with the help of an additional holey dumping mirror (DM). The residual second harmonic passed through the dumping mirror is weak and does not generate any visible sidebands. The beam in the probe arm goes through a retro-reflector mounted on a piezoelectric-translation stage that offers a step-resolution of 5 nm with closed-loop position control. Another holey mirror (RM) recombines the NIR (probe) and XUV (pump) beams, which are then focused inside a reaction microscope (ReMi) on a cold gas jet of argon. The ReMi enables coincident detection and the reconstruction of the three-dimensional momenta of the ions and electrons created during the photoionization process [13]. The interferometer was actively stabilized [14] to achieve a stability of \sim 40 as over a data acquisition time of 7 h. The stability of the interferometer was critical for the successful realization of the 3-SB scheme since the oscillation period was just 850 as.

IV. THEORETICAL APPROACH

In the theoretical part of this study, we employ the general R matrix with time dependence (RMT) method [15] to generate theoretical predictions for comparison with our experimental data. In order to calculate the necessary time-independent basis functions and dipole matrix elements, we set up the two-state nonrelativistic model introduced by Burke and Taylor [16] to treat the steady-state standard photoionization process. In this model, multiconfiguration expansions for the initial $(3s^23p^6)^1S$ bound state and the two coupled final ionic states $(3s^23p^5)^2P$ and $(3s3p^6)^2S$ were employed. We checked that the photoionization cross sections at the photon energies corresponding to the various HHG lines was reproduced properly (in agreement with Burke and Taylor [16] as well as experiments [17,18]) by our RMT model.

The probe-pulse duration was chosen as about twice the length of the XUV pulse. We emphasize that the present calculation was meant as a supplement to the current experiment, with the hope of providing additional qualitative insights rather than quantitative agreement, which would require much more detailed information about the actual pulses than what was available. We purposely employed significantly lower NIR peak intensities $(10^{11}\,\mathrm{W/cm^2})$ than in the experiment $(\sim\!6\times10^{11}\,\mathrm{W/cm^2})$. This reduced the number of partial waves needed to obtain converged results, diminished potential distortions, and thus made it easier to interpret the spectra.

Specifically, we performed calculations for 11 delays in multiples of 0.05 NIR periods. For each delay, we needed about 5 h on 23 nodes using all 56 available cores per node on the Frontera supercomputer hosted at the Texas Advanced Computing Center (TACC) [19].

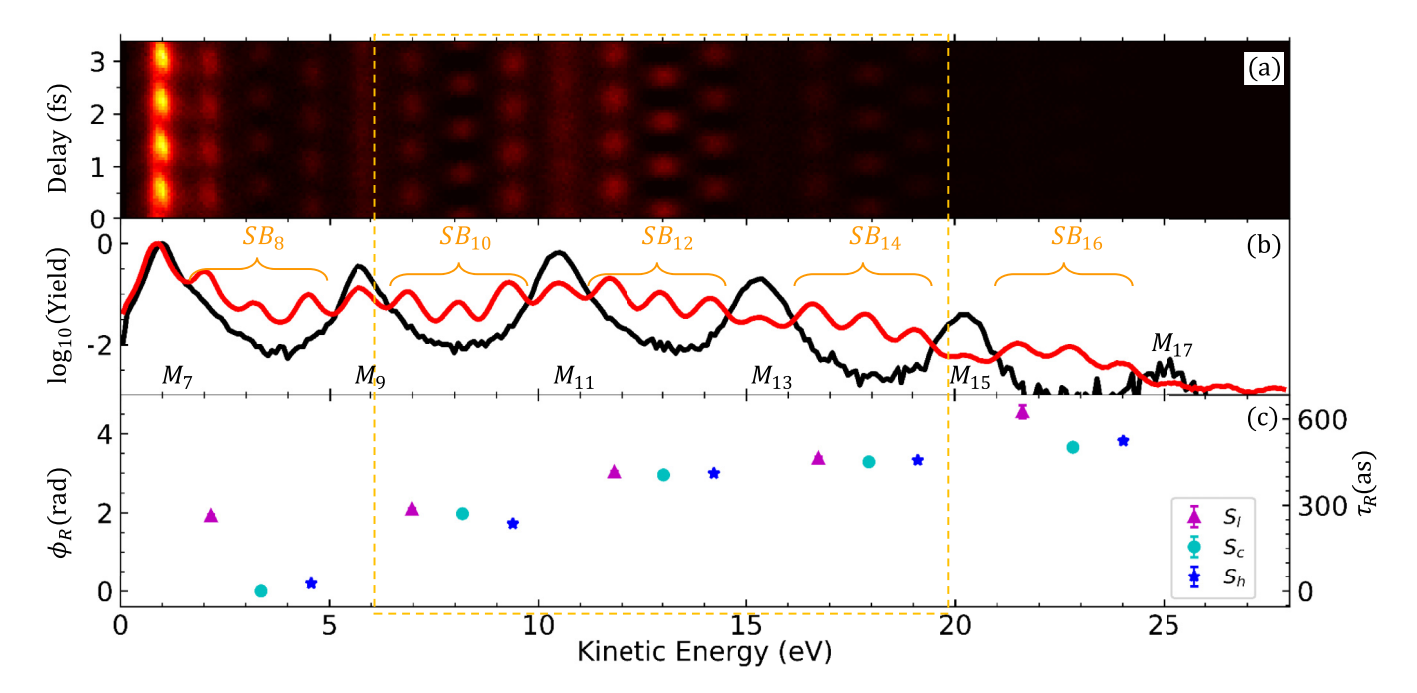


FIG. 3. (a) 3-SB RABBIT trace, (b) normalized photoelectron spectra generated with the XUV pulse only (dark) and during the RABBIT measurement integrated over the delays (lighter), and (c) RABBIT phases extracted from all three sidebands. Note that the π phase difference between S_c and (S_l, S_h) , which is clearly seen in the position of the maxima in (a), has been removed for better visibility in (c). The error bars from the fitting procedure are generally smaller than the symbol size and hence hardly visible. The dashed box from about 6 eV to 21 eV indicates the sideband groups that we concentrate on for the angle-differential cases.

V. RESULTS AND DISCUSSION

Below we present our results. We start with the angle-integrated setup in Sec. VA before going into further detail with angle-resolved measurements and calculations in Sec. VB.

A. Angle-integrated RABBIT phases

Figure 3 exhibits the results of our 3-SB RABBIT experiment after integrating the signal over all photoelectron emission angles. To highlight the oscillations, the RABBIT trace in Fig. 3(a) is plotted after subtracting the average delay-integrated signal. The delay-integrated photoelectron spectra (normalized to 1 at the highest peak) are plotted in Fig. 3(b). Due to the high NIR intensity, some of the main bands are depleted substantially and appear weaker than the SBs in their vicinity. The angle-integrated photoelectron spectrum is integrated over a spectral window of 0.7 eV around the peak of the SBs.

The RABBIT phase (ϕ_R) is extracted by fitting a cosine function [cf. Eqs. (1)] to these delay-dependent oscillating signals of the sidebands, as seen in Fig. 4. Due to the large data set available and the excellent stability of the interferometer, the phase retrieval generally resulted in error bars smaller than the symbol size in Fig. 3(c). This gives us confidence in the results obtained from our extraction procedure. The numerical values obtained for the various SB groups, as well as the contrast ratio

$$\gamma \equiv \frac{\max[SB(\tau)] - \min[SB(\tau)]}{\max[SB(\tau)] + \min[SB(\tau)]}$$
(2)

are listed in Table I. As expected, the highest contrast is found for the center sideband, due to the same (third) order of transitions involved.

We note that there are several autoionizing resonances with principal configuration $3s3p^6n\ell$ in the SB_{12} range of photoelectron kinetic energies, which converge towards the $(3s3p^6)^2S$ threshold of the first excited state of Ar⁺ around 13.5 eV [20]. Early measurements of the $(3s3p^6np)^1P^o$ resonances were reported by Madden *et al.* [21]. They were also seen by Burke and Taylor [16] in their photoionization work, and further resonances with other configurations, which can be reached by charged-particle or multiphoton impact, were discussed by Bartschat and Burke [22]. More recently, the

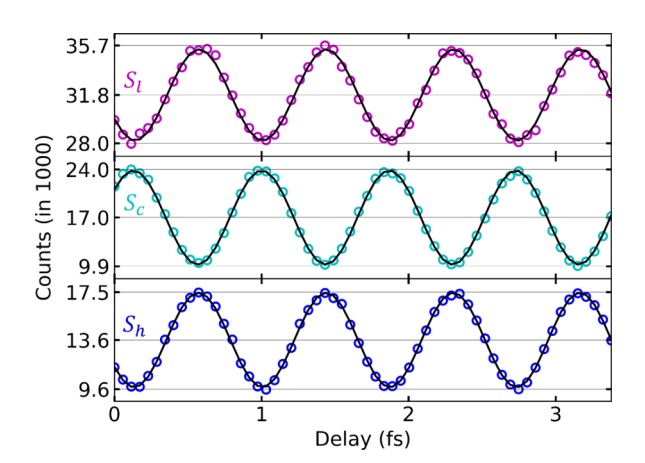


FIG. 4. The delay-dependent photoelectron signal (dots) of the three sidebands in the SB_{12} group and fits to a cosine function (lines).

	SB_8		SB_{10}		SB_{12}		SB_{14}		SB_{16}	
	ϕ_R	γ								
S_l :	1.93 ± 0.03	0.07	2.09 ± 0.02	0.11	3.03 ± 0.02	0.11	3.38 ± 0.03	0.09	4.56 ± 0.10	0.04
S_c :	0.00 ± 0.02	0.15	1.98 ± 0.01	0.36	2.96 ± 0.01	0.41	3.29 ± 0.01	0.38	3.66 ± 0.02	0.24
S_h :	0.19 ± 0.02	0.09	1.73 ± 0.02	0.10	3.00 ± 0.01	0.28	3.33 ± 0.01	0.32	3.82 ± 0.05	0.15

TABLE I. RABBIT phase extracted from the fitting procedure and the contrast γ of the oscillation.

effect of these resonances on the RABBIT phase in 1-SB setups was reported by Kotur *et al.* [23] and Cirelli *et al.* [24].

Since we used the coupled-state description of Burke and Taylor [16], we saw resonance effects in test calculations, but only with appropriate frequencies and sufficiently long pulses, for which the resonance widths could be well resolved. Note that these features are very sensitive to small fluctuations in the frequency and bandwidth of the APT during the XUV generation process. Therefore, these structures were not seen in the three experimental data points presented in the SB_{12} region. We hope to generate additional data with tunable high-order harmonic frequencies in the future. This will make it possible to investigate the resonance phenomena in more detail.

As predicted by our generalized decomposition approximation [cf. Eqs. (1)], the lower and the higher SBs oscillate by π out of phase with the central SB. The retrieved RABBIT phases ϕ_R are plotted in Fig. 3(c) after removing the extra π from S_l and S_h to simplify the comparison. The time-delay axis on the right side of this panel was created via the conversion $\tau_R = \phi_R/(4\omega)$.

Five SB groups are clearly identifiable in Fig. 3(c). While there are some irregularities in SB_8 and SB_{16} , especially with the phase extracted from S_l , groups SB_{10} , SB_{12} , and SB_{14} show the expected trend: The RABBIT phases of the three SBs in each group are similar, although a small difference remains visible in SB_{10} . That difference, however, essentially vanishes in SB_{12} and SB_{14} .

The irregularity seen in the SB_8 group is due to a significant contribution of another fourth-order transition in the absorption path of the lowest SB S_l , which involves a transition from M_7 down to the Rydberg states and back up to S_l . The Rydberg states enhance the strength of this transition and add a resonance phase that leads to a significant deviation in the RABBIT phase of S_l compared to the other members of the SB_8 group. Furthermore, due to the low cutoff of the XUV spectrum based on HHG and the decreasing photoionization cross section of argon with increasing photon energy, the strength of the M_{17} peak is very weak compared to the rest of the lower main peaks. As a result, higher-order transitions involving lower main bands also play a significant role in the oscillation of S_l in the SB_{16} group, which again affects the extracted phase.

B. Angle-differential RABBIT phases

We now further increase the level of detail by investigating angle-dependent RABBIT phases, which is possible due to the angle-resolving capability of the reaction microscope. For the reasons given above regarding the additional complexities associated with the SB_8 and SB_{16} groups, we concentrate the remaining discussion on SB_{10} , SB_{12} , and SB_{14} .

Figures 5(a)-5(c) show the RABBIT phases extracted within these groups as a function of the photoelectron emission angle, which is defined relative to the (linear) laser polarization vector. The photoelectron signal is integrated over an angular window of 10° for each data point. The angle-resolved RABBIT phases are shifted to fix the starting phase of the central sideband in each group to zero. According to both our experiment and the calculation [Figs. 5(d)-5(f)], the phase of S_h exhibits a stronger angular dependence compared to that of S_c and S_l . With increasing photoelectron energy, the differences diminish in both experiment and theory, with theory predicting almost no angle dependence in the range of SB_{14} plotted.

To explain the angle dependence in the RABBIT phase, we need to consider the interference among all the angular-momentum channels of the sidebands accessed through the absorption and emission paths. We write the signal in compressed form as

$$S_{q}(\tau,\theta) \propto \sum_{\ell,\ell',m} \alpha_{\ell,m}^{a} \alpha_{\ell',m}^{e^{*}} Y_{\ell,m}(\theta) Y_{\ell',m}^{*}(\theta)$$

$$\times \cos\left(4\omega\tau - \Delta\phi_{\Omega}^{q} - \Delta\phi_{\ell\ell',m}^{at}\right)$$

$$\propto I_{1}(\theta) \cos[4\omega\tau - \phi_{R}(\theta)]. \tag{3}$$

Here α^a and α^e are the transition amplitudes involving the various fields and matrix elements, while $\ell(\ell')$ denotes the angular-momentum channels accessed through the absorption (emission) paths.

The dissimilarity in the RABBIT phases $[\phi_R(\theta)]$ of the three SBs can be explained by considering a propensity rule for the transition amplitudes and the dependence of both the Wigner and ϕ^{cc} phases on the orbital angular momenta. It is well known that the Wigner phase depends on the angular momentum channel. The cc phase has also been shown to depend slightly on whether there is an increase or decrease in the angular momentum, while it appears to remain independent of the target species [25,26]. Therefore, the atomic phases $(\Delta \phi_{\ell\ell',m}^{\rm at})$ arising from the interference between various ℓ channels in the emission and absorption paths are also expected to differ. Similar to bound-continuum transitions [27], absorption (emission) within the continuum favors an increase (decrease) in the angular momentum of the outgoing photoelectron, especially for low kinetic energies [26,28–31]. The higher SB (S_h) of the group involves the absorption of three probe photons $(H_{q-1} + 3\omega)$ that, according to the propensity rule, predominantly populate higher angularmomentum states. Along the other path $(H_{q+1} - 1 \omega)$ leading

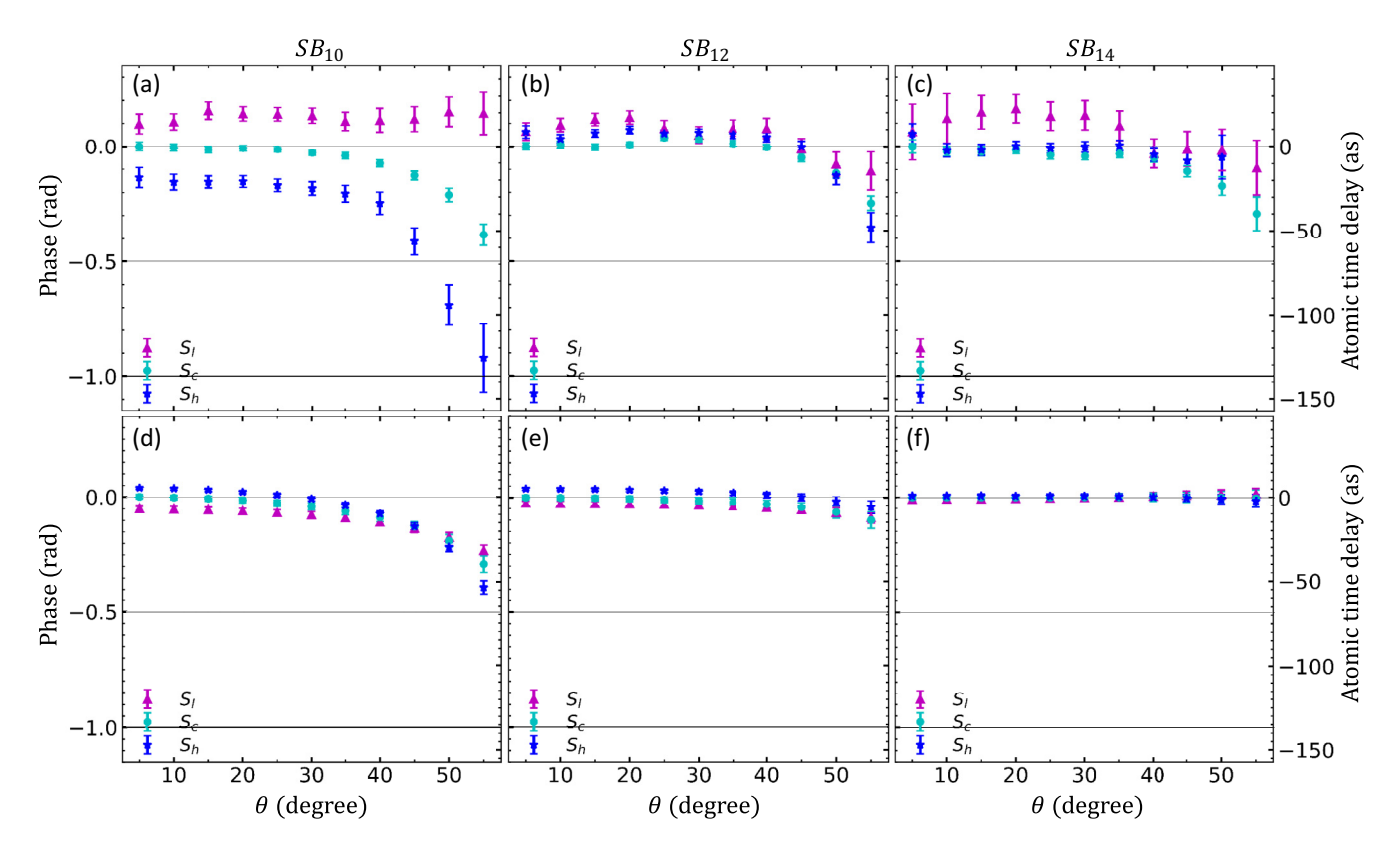


FIG. 5. Top row: Angle-dependent RABBIT phases extracted from the measurements in group (a) SB_{10} , (b) SB_{12} , and (c) SB_{14} . Bottom row: Corresponding RMT predictions.

to S_h , the emission of one probe photon mainly creates lower angular-momentum states. For S_l , emission of three probe photons $(H_{q+1}-3\omega)$ primarily leads to the population of lower angular-momentum states. Even though the absorption path $(H_{q-1}+1\omega)$ to S_l also favors an increase in the photoelectron's angular momentum, the possible values reached by the absorption of a single probe photon remain relatively small.

The interplay of the propensity rule for transition amplitudes to each ℓ channel and the angle-dependent amplitudes of the coupled spherical harmonics determine the angular variation of ϕ_R in the three SBs. In cross-channel interference, $\ell \neq \ell'$, the angle-dependent spherical harmonics undergo a sign change across their angular nodes, thus resulting in a phase jump by π . If the relative magnitude of these cross-channel interferences is significant compared to that of the same-channel interference terms, $\ell = \ell'$, this can lead to a rapid variation in the angle dependence of ϕ_R in the vicinity of the nodes [29]. Depending on the value of $\Delta \phi_{\ell\ell',m}^{\rm at}$ relative to the average $\Delta \phi^{\rm at}$ of the interference terms, the additional π jump at the nodes in $Y_{\ell,m}$ and/or $Y_{\ell',m}$ can drive the angle-dependent curve downward or upward.

With increasing ℓ value, the position of the first node in the associated Legendre polynomial of the spherical harmonic moves to smaller angles. Due to the propensity rule, the weight of the cross-channel interference term containing large ℓ values is most significant in the higher sideband. This results in a relatively early onset of the descent in the angle-dependent RABBIT phase in the higher sideband. In the lower

sideband, the amplitude of the cross-channel interference term containing large ℓ values is not very strong; hence, the π jump across the node does not produce a substantial change in the overall retrieved phase. With increasing kinetic energy, for both the absorption or emission of the probe photons, the transition amplitudes for increasing and decreasing angular momentum tend to become similar [29]. Hence, the contribution of cross-channel interference containing large ℓ values decreases with increasing kinetic energy. Thus the π jumps at the nodes of the corresponding spherical harmonics do not change the retrieved phase significantly.

Since the retrieved angle-integrated RABBIT phase is the weighted average of all the channel-resolved RABBIT phases and the weights of these channels in the S_l , S_c , and S_h SBs are different, the angle-integrated RABBIT phase in the three SBs also turns out different. Also, owing to the propensity rule, the unequal transition probabilities of reaching the various angular—momentum states of the SBs in absorption and emission of the probe photons may cause incomplete interference in the individual ℓ channels, thereby reducing the overall oscillation contrast in the angle-integrated photoelectron signal.

Finally, we notice that the scale of the variations in the angle-dependence of the RABBIT phase depicted in Fig. 5 is smaller in the calculation than in our experiment. Also, the positions of S_l and S_h relative to S_c appear to be switched. In addition to always possible shortcomings in the theoretical model (as sophisticated as it might be) and unknown potential systematic errors in the experiment, the differences in the probe intensities and the pulse details, in general, are likely

responsible for at least some of the discrepancies seen here. We hope to be able to investigate this in more detail in the future by performing additional calculations with different intensities and more time delays.

VI. SUMMARY AND OUTLOOK

In summary, we carried out a proof-of-principle 3-SB RABBIT experiment in argon. In contrast to more popular single-SB studies, our technique enables us to focus on the photon-induced transition phases without distortion from a possibly unknown or experimentally drifting XUV chirp. While we confirmed earlier predictions that the angle-integrated RABBIT phases extracted within a SB group become increasingly similar, we enhanced the analyzing power of the setup significantly by resolving the emission angle with a reaction microscope. By doing so, we could identify which of the three sideband phases within a group is most sensitive to a change in the detection angle.

Our experimental efforts were accompanied by numerical calculations performed with the nonperturbative all-electron *R* matrix with time dependence method. There is some qualitative agreement between experiment and theory regarding the general trends observed, but significant differences remain in the details. Given the remaining limitations and challenges faced in the present study, especially concerning the details of the pulse and the argon target, the remaining deviations between experiment and theory in the quantitative values of the phases are not too surprising. We hope to address these issues in future improvements of the setup.

As the next step, we plan to repeat this experiment with helium, where the contribution of the Wigner phase for an $s \rightarrow p$ transition remains the same in all three sidebands.

Any differences in the phases within the group then clearly indicate the influence of ϕ^{cc} . This switch of targets will require extending the harmonic cutoff, which is by no means trivial in our scheme, as the cutoff in the HHG process decreases with the driving frequency. Using helium instead of argon also has the advantage of theory likely being more reliable due to the simplicity of the target. On the other hand, heavier quasi-two-electron targets with an $(ns^2)^1S$ outer-shell configuration (unfortunately, these are metals that would need to be vaporized rather than inert gases) would provide a larger short-range modification of the relevant interaction potential and therefore may be more suitable to investigate whether ϕ^{cc} is indeed nearly universal.

Undoubtedly, many open questions will need to be answered before the effects of the additional continuum-continuum transitions in single- and multi-SB RABBIT setups are fully understood. It would be interesting to analyze whether the SB phases always converge to each other with increasing energy, whether or not they cross in a predictable way with increasing emission angle, and how the behavior depends on the target investigated. While we cannot answer these questions at the present time, we hope that other groups will see the work reported in this paper as a worthwhile inspiration to carry out further studies in this field.

ACKNOWLEDGMENTS

The experimental part of this work was supported by the DFG-QUTIF program under Project No. HA 8399/2-1 and IMPRS-QD. K.R.H. and K.B. acknowledge funding from the NSF through Grants No. PHY-1803844 and No. PHY-2110023, respectively, as well as the Frontera Pathways allocation PHY-20028.

- [1] P. M. Paul, E. S. Toma, P. Breger, G. Mullot, F. Augé, P. Balcou, H. G. Muller, and P. Agostini, Science **292**, 1689 (2001).
- [2] H. G. Muller, Appl. Phys. B 74, s17 (2002).

^[3] K. Klünder, J. M. Dahlström, M. Gisselbrecht, T. Fordell, M. Swoboda, D. Guénot, P. Johnsson, J. Caillat, J. Mauritsson, A. Maquet, R. Taïeb, and A. L'Huillier, Phys. Rev. Lett. 106, 143002 (2011).

^[4] E. P. Wigner, Phys. Rev. 98, 145 (1955).

^[5] J. M. Dahlström, A. L'Huillier, and A. Maquet, J. Phys. B: At. Mol. Opt. Phys. 45, 183001 (2012).

^[6] J. M. Dahlström and E. Lindroth, J. Phys. B: At. Mol. Opt. Phys. 47, 124012 (2014).

^[7] R. Pazourek, S. Nagele, and J. Burgdörfer, Rev. Mod. Phys. 87, 765 (2015).

^[8] V. Loriot, A. Marciniak, G. Karras, B. Schindler, G. Renois-Predelus, I. Compagnon, B. Concina, R. Brédy, G. Celep, C. Bordas, E. Constant, and F. Lépine, J. Opt. 19, 114003 (2017).

^[9] S. D. López, S. Donsa, S. Nagele, D. G. Arbó, and J. Burgdörfer, Phys. Rev. A 104, 043113 (2021).

^[10] P. K. Maroju, C. Grazioli, M. Di Fraia, M. Moioli, D. Ertel, H. Ahmadi, O. Plekan, P. Finetti, E. Allaria, L. Giannessi *et al.*, Nature (London) 578, 386 (2020).

^[11] A. Harth, N. Douguet, K. Bartschat, R. Moshammer, and T. Pfeifer, Phys. Rev. A 99, 023410 (2019).

^[12] D. Bharti, D. Atri-Schuller, G. Menning, K. R. Hamilton, R. Moshammer, T. Pfeifer, N. Douguet, K. Bartschat, and A. Harth, Phys. Rev. A 103, 022834 (2021).

^[13] J. Ullrich, R. Moshammer, A. Dorn, R. Dörner, L. P. H. Schmidt, and H. Schmidt-Böcking, Rep. Prog. Phys. 66, 1463 (2003).

^[14] H. Srinivas, F. Shobeiry, D. Bharti, T. Pfeifer, R. Moshammer, and A. Harth, Opt. Express 30, 13630 (2022).

^[15] A. C. Brown, G. S. Armstrong, J. Benda, D. D. Clarke, J. Wragg, K. R. Hamilton, Z. Mašín, J. D. Gorfinkiel, and H. W. van der Hart, Comput. Phys. Commun. 250, 107062 (2020).

^[16] P. G. Burke and K. T. Taylor, J. Phys. B: At. Mol. Phys. 8, 2620 (1975).

^[17] G. Marr and J. West, At. Data Nucl. Data Tables 18, 497 (1976).

^[18] J. Samson and W. Stolte, J. Electron Spectrosc. Relat. Phenom. 123, 265 (2002).

^[19] https://www.tacc.utexas.edu/systems/frontera

^[20] A. Kramida, Yu. Ralchenko, J. Reader, and NIST ASD Team, NIST Atomic Spectra Database (ver. 5.10) [Online]. Available: http://physics.nist.gov/asd National Institute of Standards and Technology, Gaithersburg, MD (2022).

^[21] R. P. Madden, D. L. Ederer, and K. Codling, Phys. Rev. 177, 136 (1969).

- [22] K. Bartschat and P. G. Burke, J. Phys. B: At. Mol. Opt. Phys. 21, 2969 (1988).
- [23] M. Kotur, D. Guénot, Á. Jiménez-Galán, D. Kroon, E. W. Larsen, M. Louisy, S. Bengtsson, M. Miranda, J. Mauritsson, C. L. Arnold, S. E. Canton, M. Gisselbrecht, T. Carette, J. M. Dahlström, E. Lindroth, A. Maquet, L. Argenti, F. Martín, and A. L'Huillier, Nat. Commun. 7, 10566 (2016).
- [24] C. Cirelli, C. Marante, S. Heuser, C. L. M. Petersson, Á. J. Galán, L. Argenti, S. Zhong, D. Busto, M. Isinger, S. Nandi, S. Maclot, L. Rading, P. Johnsson, M. Gisselbrecht, M. Lucchini, L. Gallmann, J. M. Dahlström, E. Lindroth, A. L'Huillier, F. Martín et al., Nat. Commun. 9, 955 (2018).
- [25] J. Fuchs, N. Douguet, S. Donsa, F. Martin, J. Burgdörfer, L. Argenti, L. Cattaneo, and U. Keller, Optica 7, 154 (2020).

- [26] J. Peschel, D. Busto, M. Plach, M. Bertolino, M. Hoflund, S. Maclot, J. Vinbladh, H. Wikmark, F. Zapata, E. Lindroth, M. Gisselbrecht, J. M. Dahlström, A. L'Huillier, and P. Eng-Johnsson, Nat. Commun. 13, 5205 (2022).
- [27] U. Fano, Phys. Rev. A 32, 617 (1985).
- [28] M. Bertolino, D. Busto, F. Zapata, and J. M. Dahlström, J. Phys. B: At. Mol. Opt. Phys. 53, 144002 (2020).
- [29] D. Busto, J. Vinbladh, S. Zhong, M. Isinger, S. Nandi, S. Maclot, P. Johnsson, M. Gisselbrecht, A. L'Huillier, E. Lindroth, and J. M. Dahlström, Phys. Rev. Lett. 123, 133201 (2019).
- [30] A. S. Kheifets, Phys. Rev. A 105, 013114 (2022).
- [31] D. I. R. Boll, L. Martini, and O. A. Fojón, Phys. Rev. A 106, 023116 (2022).